Confining invasion directions of Li+ to achieve efficient Si anode material for lithium-ion batteries

Ziqi Zhang[a], Huiqiong Wang[a], Meijuan Cheng[a], Yang He[c], Xiang Han[d], Linshan Luo[a], Pengfei Su[a], Wei Huang[a], Jianyuan Wang[a], Cheng Li[a], Zizhong Zhu[a,*], Qiaobao Zhang[b,*], Songyan Chen[a,*]

[a] Department of Physics, Jiujiang Research Institute and Collaborative Innovation Center for Optoelectronic Semiconductors and Efficient Devices, Xiamen University, Xiamen 361005, China
[b] Department of Materials Science and Engineering, College of Materials, Xiamen University, Xiamen, Fujian 361005, China
[c] Beijing Advanced Innovation Center for Materials Genome Engineering, University of Science and Technology Beijing, Beijing, 100083, China
[d] College of Materials Science and Engineering, Nanjing Forestry University, Nanjing, 210037, China

ARTICLE INFO

ABSTRACT

Tremendous volume expansion of silicon anode during cycling limits its further application. Here, a novel silicon nano-ribbon (SiNR) with (110) crystal plane is proposed as anode for the Lithium-ion batteries. The SiNRs with (110) crystal plane have been synthesized by a simple electrochemical micromachining method. Both invasion direction of the lithium-ions and expansion directions of the lithiated silicon are limited to the <110> crystal direction. Recrystallization of SiNR induced by the retention of silicon atomic chains after delithiation is verified experimentally and theoretically. Such SiNR, without necessary surface coating treatment, exhibits high ionic conductivity, high stable solid electrolyte interphase (SEI) and long cycling stability, retaining a specific capacity of 1721.3 mAh g^{-1} (∼80% capacity retention) after 2000 cycles with an initial coulombic efficiency (CE) of 83%. The rational design of nanostructured battery materials and electrodes in this work also opens a new dimension in material design for other batteries.

1. Introduction

The development of lithium ion battery with high specific energy and high specific power has become a key scientific and technological challenge [1–4]. Theoretical calculation shows that increasing the capacity of anode makes a great contribution to improving energy density of battery if the capacity of anode is below 1200 mAh g^{-1} [5]. Improving the anode performance is undoubtedly a simply effective way to develop advanced lithium-ion batteries (LIBs). Silicon anode has been considered as one of the promising candidates in advanced LIBs due to its high theoretical capacity of 3579 mA h g^{-1} (Li$_{15}$Si$_4$) at room temperature [6,7]. However, similar to other high capacity anode materials [8,9], silicon anode has some bottleneck problems that limit its further application: tremendous volume expansion of silicon during cycling results in particle pulverization and unstable solid electrolyte interphase (SEI), which causes rapid capacity fading [10–12].

The size of silicon particles in anode has a huge impact on its electrochemical performance [13]. Smaller Si particles have lower probability of cracking, shorter migration path for lithium ions and bigger free space to accommodate volume change during cycling [14,15]. Conse-

quently, a number of previous studies have been focused on micro-nano structures of silicon anode, such as silicon nanowires [16–18], silicon nanotube [19], silicon film [20,21], core-shell structure [22,23], porous silicon [24,25], etc. Through micro-nanometer process, the mechanical stability has been greatly improved. Regretfully, the expansion of silicon anode during lithiation proved to be irrepressible both theoretically and experimentally. For micro-nano Si anode with a large specific surface area, the impact of expansion is even worse: the side reactions are aggravated, leading to a continuously thickening SEI [26] (Fig. 1a). To achieve a stable SEI, extra surface coating for Si anodes is usually demanded. The coating material could be flexible or tough to accommodate the stress, conductive to construct electronic and ionic transport channels, electrochemically stable to protect silicon from electrolyte. Many materials, such as carbon [27,28], Al$_2$O3 [29], TiO2 [30], Co3O4 [31], Al [32], etc, have been investigated extensively for their outstanding integrated performances.

Through theoretical calculation and *in situ* characterization techniques, the physical basis of microstructural evolution, morphological changes and mechanical degradation in silicon-based electrodes during cycling has been thoroughly investigated. The volume change of the
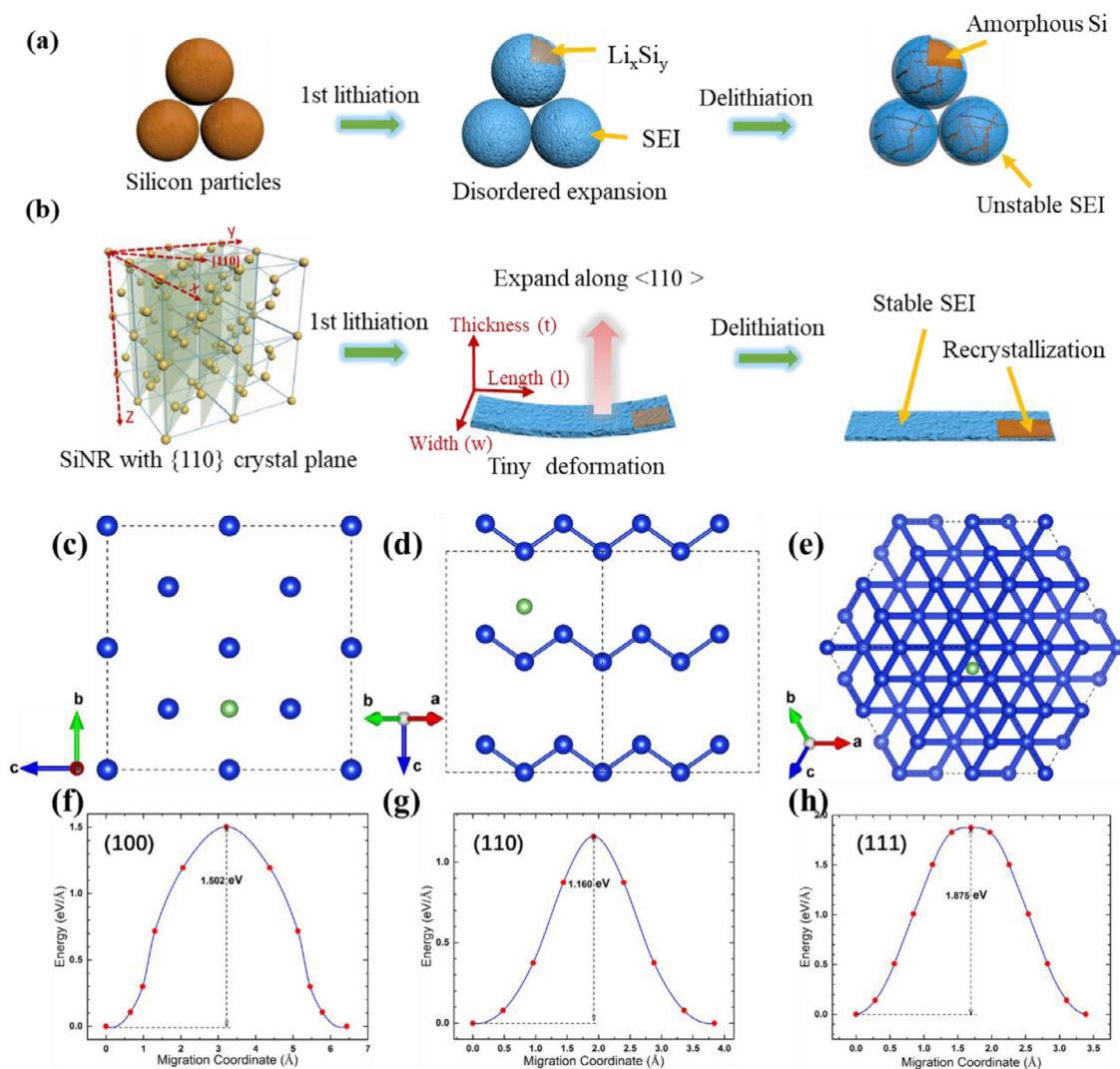
Fig. 1. Schematic diagram of ordinary silicon anode material (a) and silicon nano-ribbon (SiNR) anode (b) during the first Lithiation/Delithiation process. Li$^+$ migration channels in the bulk Si viewed along <100> direction (c), <110> direction (d) and <111> direction (e). The calculated vacancy migration barriers of the bulk Si along <100> direction (e), <110> direction (f) and <111> direction (g).

lithiated silicon electrode is approximately 300%, which has a linear relationship with lithium content [33,34]. The lithiation kinetics in crystal silicon has been verified to be anisotropic; this process is accompanied by a phase transition and mechanical properties change [35–38]. The rate of lithiation/ delithiation depends strongly on the invasion direction of the lithium, with <111> reported to be the slowest and <110> to be the fastest [39–41]. Even the corresponding dynamic lithiation process of crystal silicon with atomic resolution has been observed by *in situ* transmission electron microscopy [42]. Inspired by the magical relationship between the orientation of crystals and the direction of expansion, a question was raised as to: can we achieve stable Si anodes by synergistically adjusting the crystal orientation and structural geometry? We then carried out theoretical and experimental research to optimize the Si anode electrochemical properties through tuning of crystal orientation.

2. Results and discussion

Fig. 1 illustrates the atomic models of Li$^+$ migration channels in the bulk Si along <100> (Fig. 1c), <110> (Fig. 1d) and <111> (Fig. 1e) directions. We firstly performed first principle calculations to compare the vacancy migration barriers along the different orientations and the calculated results are 1.502 eV (Fig. 1f), 1.160 eV (Fig. 1g) and 1.875 eV (Fig. 1h), respectively. The migration along the <110> direction re-

quires the lowest amount of energy, which is about 77.2% of that along the <100> direction, and 61.9% of that along the <111> direction. Therefore, confining the transporting direction of the majority of Li$^+$ along the <110> direction is expected to greatly improve the speed and efficiency of lithium intercalation/ deintercalation. Although tremendous volume expansion of silicon causes an unstable SEI [43–46], the preferential volume expansion along <110> direction ensures a constant area of (110) crystal plane, namely a naturally stable SEI on (110) crystal plane (Method S1). Hence, enlarging the (110) crystal surface of silicon anode will make full use of the advantage of crystalline orientation. On the other hand, in order to minimize the effect of volume expansion along <110> on the remaining crystal surface and the whole electrode, it is desirable to reduce the thickness of (110) Si anode to nanoscale. Here, a novel quasi two-dimensional silicon nano-ribbon with (110) crystal plane (SiNR) is adopted as anode in this work (Fig. 1b). The large (110) crystal interface of SiNR allows the majority of Li$^+$ to transport along the <110> direction. As we will show in details later, our experiments demonstrate that, during lithiation, the SiNR slightly thickens along t axis while keeping the original thickness along l or w-axis, which is crucial to keep a stable SEI. Due to an extremely short diffusion distance and a higher speed lithium ion diffusion channel along the <110> direction, the SiNR electrode performs an extremely high rate performance. Even
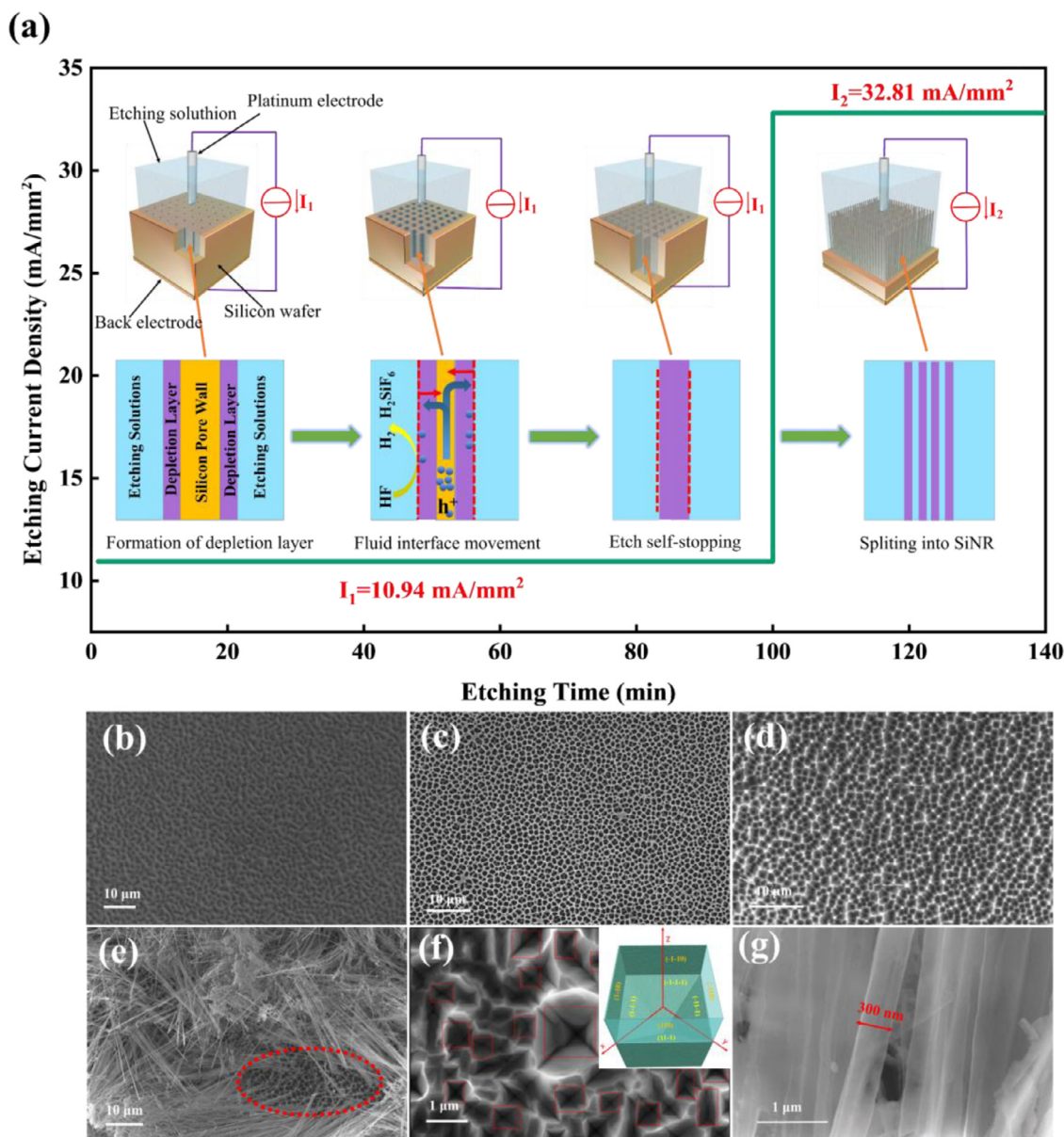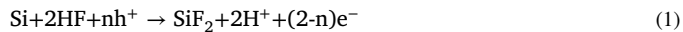
Fig. 2. The evolution of silicon nanoribbon (SiNR) in an electrochemical etching process. (a) Schematic diagram of the evolution mechanism for SiNR from a silicon substrate. The morphology of silicon substrate probed by SEM after 10 min (b), 25 min (c), 40 min (d) and 140 min (e) in the electrochemical etching process. (f) Inverted pyramidal pits at the roots of silicon nanoribbons (corresponding to the area indicated by red dashed circle in Fig. 2e). (g) Silicon nanoribbon arrays with high magnification.

more interestingly, recrystallization of silicon anode after delithiation is observed, which is helpful to keep a stable crystal structure, maintaining its property of directional expansion and assuring the excellent cycling reversibility.

To synthesize the SiNR, P-type silicon (100) wafers were used as substrates. Secondary electron microscopy (SEM) was used to exam the evolution of morphology during the electrochemical corrosion process (Fig. 2a). There appeared circular pores first (Fig. 2b), which were enlarged gradually (Fig. 2c) and finally squeezed to square (Fig. 2d). A depletion layer was formed at the interface between corrosive liquid and pore wall, where stoichiometric reactions occured as follows:

$$Si + 2HF + nh^+ \rightarrow SiF_2 + 2H^+ + (2-n)e^- \quad (1)$$

$$SiF_2 + 2HF \rightarrow SiF_4 + H_2 \quad (2)$$

$$SiF_4 + 2HF \rightarrow H_2SiF_6 \quad (3)$$

Under the action of electric field (constant current $I_1 = 10.94$ mA/mm^2), the hole carriers migrated from the bottom of the substrate along the longitudinal pore walls to the interface and participated in the reaction, during which the pore walls gradually thinned. This lateral self-limiting electrochemical reaction finally stopped when the thickness of the wall between two adjacent holes is close to the depletion layer (< 30 nm); while the longitudinal corrosion was continuous, accompanied by an increased length of the holes. As the etching current was increased to $I_2 = 32.81$ mA/mm^2, a ribbon-like structure peeled off from the substrate and thus the SiNR was successfully synthesized (Fig. 2e). Similar to the lithiation process of silicon, the electrochemical etching process is also anisotropy. SEM images demonstrate that the etch pits at the root of SiNR prefer to be inverted pyramidal with four (111) inner surfaces (Fig. 2f). Since SiNR is perpendicular to the (100) surface and derives from the common boundaries squeezing of two adjacent square pyramid, the crystal plane
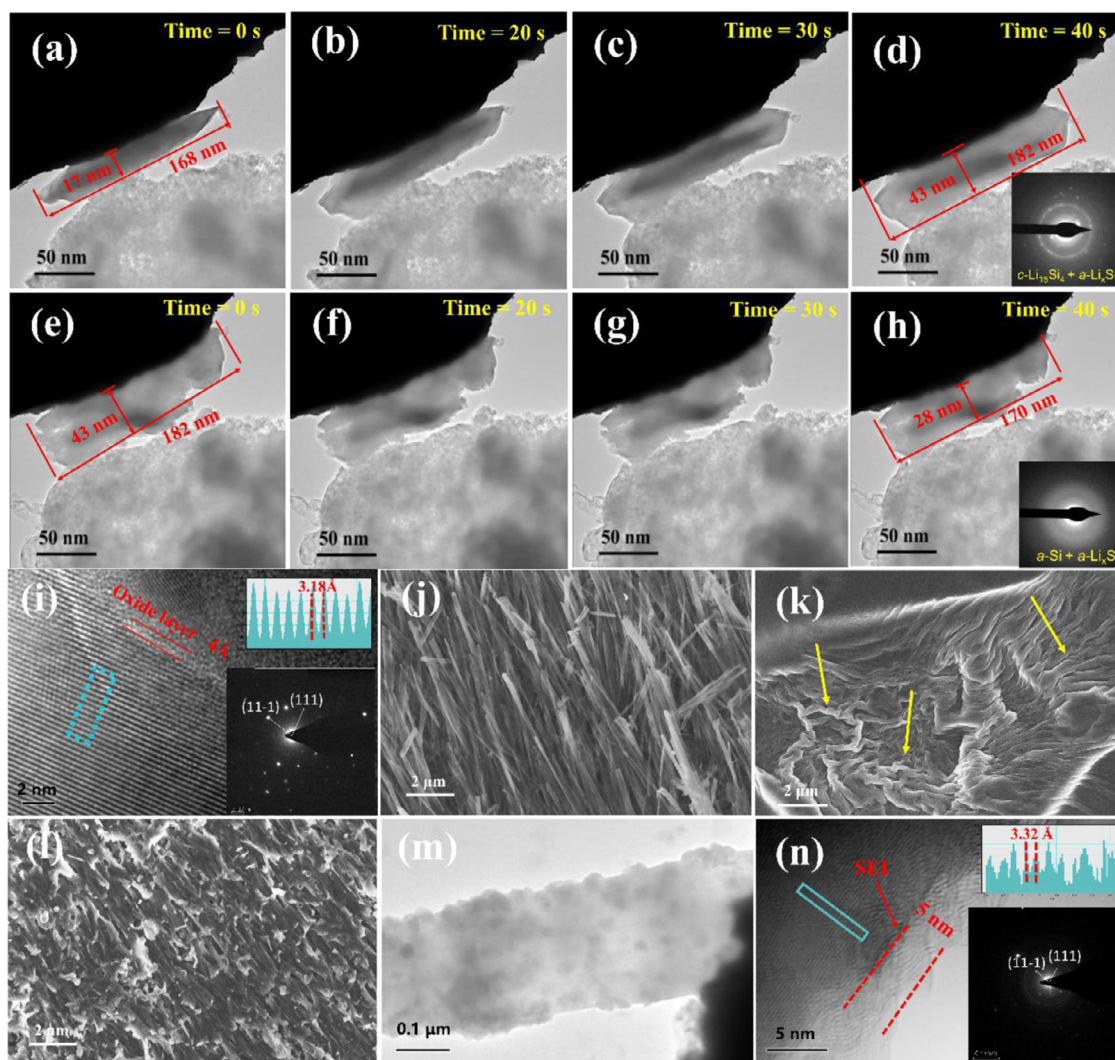
Fig. 3. Sequential *in situ* TEM snapshots showing the lithiation process of the SiNR at (a) 0 s, (b) 20 s, (c) 30 s, (d) 40 s, and the delithiation process of SiNR at (e) 0 s, (f) 20 s, (g) 30 s, (h) 40 s, respectively. (i) HRTEM images of SiNR. The insets in (d, e, h) show the corresponding electron diffraction pattern. (j) SEM image of the SiNR electrode. (k) SEM image of the SiNR electrode after the first lithiation. (l) SEM image of the SiNR electrode after the first delithiation. (m,n) TEM images of silicon nanoribbons after 100 cycles; the inset shows the corresponding electron diffraction pattern indicating the recrystallization process.

of SiNR is recognized as (110) (inset of Fig. 2f). The as-obtained SiNRs with a size of 100 μm long and 300 nm wide distribute uniformly on the substrate (Fig. 2g).

To gain a deep understanding of lithiation / delithiation dynamics, we performed *in situ* transmission electron microscopy (TEM) experiment (the schematic diagram of the corresponding experimental setup is shown in Fig. S1). An amorphous carbon layer of 1 nm was coated on SiNR (SiNR@C) by chemical vapor deposition process to ensure high conductivity and easier lithiation. The carbon layer has negligible effect on the dynamic process of expansion. The SiNR@C was attached on a gold tip and rotated until its cross section was parallel to the screen. Then the (110) crystal plane was connected to Li/Li$_2$O on a tungsten (W) tip. The thin Li$_2$O layer on Li worked as a solid electrolyte. The lithiation of SiNR took place when a negative bias (-3 V) was applied to the W end. As shown in Video S1 and Fig. 3a, the initial thickness and breadth of SiNR were 17 nm and 168 nm respectively. When Li source came in close contact, Li ions diffused quickly to the SiNR along with the noticeable increasing thickness (Fig. 3b–d). The thickness of SiNR was measured to be 43 nm (250 % of the initial thickness) after 40 s, while the breadth of SiNR increased slightly from 168 nm to 182 nm (only 8.6% of the initial thickness) (Fig. 3d). Meanwhile, no camera

focus change was observed for the TEM image during lithiation, meaning that there was no significant increase of thickness along the normal direction of the cross section. It is thus concluded that, the SiNR has undergone preferential expansion along the t-axis of SiNR while keeping the original thickness along l or w-axis during lithiation. The volume of SiNR is calculated to expand by nearly three times, consistent with the previous studies [47–51], during which it remains ribbon-like structure and shows the minimum surface area increment. The delithiation process of SiNR was realized by applying a positive bias. Likewise, as shown in Video S2, the SiNR evenly shrinks with thickness decreasing from 43 nm to 28 nm (Fig. 3e-h), with little size change in other directions, demonstrating its excellent structural reversibility.

As shown in the High Resolution TEM (HRTEM) images of the SiNR in Fig. 3i, the spacing of the lattice fringe is 3.18 Å, consistent with the (111) crystal plane spacing of silicon. A native oxide layer of 2 Å was coated on the SiNR. To study the morphology evolution of SiNR during (de)lithiation, working electrode (WE) of SiNR was prepared by sputtering electrode and tearing-off method. The ribbon-like structure was well maintained and vertically distributed on the initial electrode (Fig. 3j). After the initial lithiation, the SiNR slightly thickened while no significant changes in length or width were observed (Fig. 3k), which

was crucial for a stable SEI. Additionally, a minor bend of the lithiated SiNR was observed (see the yellow arrows in Fig. 3k), which was related to the effective stress release. After delithiation, the SiNR thinned back, close to the initial state (Fig. 3l). For comparison, the SiNP electrode was found to undergo uniform expansion during the first lithiation. The SiNPs in our work are specially selected to compare with SiNR. The average diameter of the SiNPs is about 20 nm (Figure S7 a), close to the thickness of the SiNRs, which ensures that Li^+ transport distance in the two Si anode is similar. Meanwhile, the crystalline state and surface state of the two are also similar. The SiNPs are single crystals and coated with a 5 nm thick oxide layer (Figure S7 b). A thick SEI was formed after the first cycle, demonstrating violent side effects on the interface of SiNP (Figure S2). The TEM images of SiNR after 100 cycles are provided in Fig. 3 m-n. Despite repeated expansion and contraction of SiNR, the ribbon-like structure is still clearly visible. From Fig. 3m, a stable SEI with a thickness of 5 nm was evenly coated on SiNR. It is worth mentioning that no surface coating is applied to the SiNR. Even more interestingly, the lattice fringe remains evident with a spacing of 3.32 Å, slightly larger than that in the original SiNR. It demonstrates that the interatomic spacing increases between Si (110) plane, while keeps original inside the Si (110) plane. We speculate that recrystallization of SiNR occurs in the delithiation process.

To figure out the crystal structure evolution of SiNR during cycling, both SiNR (Fig. 4a) and SiNP (silicon nanoparticles) (Fig. 4b) during the first cycle were analyzed by *in situ* X-ray diffraction. Both samples showed typical Bragg reflections of Si before cycling. For SiNR (Fig. 4a), there gradually appeared peaks of Li-Si alloy at 26.8 º, 38.4º and 44.7º when lithiation occurs, close to those of Si, indicating that the Li-Si alloy has a similar phase structure with that of Si. With the increase of lithium intercalation degree, the peak intensity of Li-Si alloy gradually increased. At the same time, the Si diffraction peak became weaker and wider, with a slow peak shift of Si (220) towards smaller angles (Fig. 4c). This means that the (110) crystal plane spacing increased, in accord with the directional constrained expansion of SiNR, during which the Li ions are embedded in the interlayer space of (110) crystal plane and bond with Si atoms. About ten hours later, the lithiation process is completed. The peak intensity of Li-Si alloy as well as the offset of Si (220) peak reached their maximum. The Li-Si peaks are centralized and sharp, demonstrating a nearly perfectly ordered crystal structure between Si and Li. We can conclude that limiting the invasion direction of Li^+ along <110> helps to keep the stability of atomic arrangement. The maximum angle offset of Si (220) is 0.236º. It is worth noting that during delithiation, the Si (220) peak slowly shifted back to high angles, accompanied by an enhanced peak intensity, demonstrating a reversible crystal structure of SiNR. This phenomenon is probably related to the recrystallization of SiNR in the process of delithiation, which has good agreement with the TEM results (Fig. 3n). In contrast, for SiNP (Fig. 4b), the newly generated peaks of Si-Li alloy present a dispersive feature, ranging from 34.6º to 40.8º, and 45.3º to 46.6º, indicating an amorphous phase. And there is no visible peak at around 26.8º. Neither significant angle shift nor enhanced peak of Si is observed (Fig. 4d). The SiNP tends to expand uniformly in all directions (Figure S2b).

To understand the mechanism of recrystallization for SiNR at the atomic level, the structural evolution of SiNR during the lithiation/delithiation processes have been simulated by the first-principles calculations. The results (see Fig. 4e-m) show clear structure changes during the Li insertion, which can be easily understood by the following mechanism: the more Li atoms intercalated, the more Si-Si bonds broken. Fig. 4e shows the SiNR before lithiation; when only a very small number of Li atoms are inserted (*e.g.* $Li_{0.4}Si_4$), none of the Si-Si bonds is broken (Fig. 4f); when lithiation is further increased (*e.g.* $Li_{4.2}/Si_4$), some broken Si-Si bonds start to appear (Fig. 4g). When more Li atoms are intercalated (*e.g.* $Li_{6.5}/Si_4$), it can be seen that all the Si-Si bonds between one of the Si-Si layers are totally broken (Fig. 4h), indicating that Si-Si bonds between the Si-Si layers are easier to break than those inside the Si(110) layers. When the insertion of Li is further increased (*e.g.*

$Li_{6.5}/Si_4$), the Si-Si bonds between all the Si-Si layers are broken, leading to a two-dimensional square-like structure of Si lattice, as shown in Fig. 4(i)-(j). When the Li intercalations reach $Li_{8.4}/Si_4$, the Si-Si bonds in the square-like lattice are gradually further broken, leading to the chain structure of Si, as shown in Fig. 4(k)-(l). Further intercalation of Li will gradually break the Si-Si bonds in the chain structure, finally leading to the structure of Li_{15}/Si_4 (see Fig. 4m), reaching the maximum amount of Li intercalation in the Si(110) slab, which is also the maximum amount of embedded lithium in bulk Si [52,53].

The delithiation is the reversing process to the lithiation in the above theoretical calculations. Since the present first-principles calculations are performed at T = 0 K which is time-independent, the lithiation and delithiation are the same in the present computational model. That is, the Si-Si chains seek other Si-Si chains to bind and form the square-like structure, during the delitiation. The square-like structure of Si then forms SiNR slab structure during the further lithiation. When Li are fully extracted, all the Si-Si broken bonds will disappear. This structural evolution of SiNR during the Li lithiation/delithiation process explains the special recrystallization and excellent cycling stability of SiNR as anode material in our experiment, as well as the high energy density of the system.

Cycling performance of SiNR and SiNP at 0.1 C was measured respectively in a coin-cell configuration with a lithium metal as the counter electrode in Fig. 5a. The corresponding galvanostatic charge/ discharge profile for the first cycle is provided in Fig. 5b. Despite no interfacial coating modification, the SiNR electrode retains a specific capacity of 1233 mAh g^{-1} after 200 cycles. In comparison, with a degraded crystal structure of SiNP and a repeated side reactions of the interface, the recycling capacity of SiNP fades quickly, with only 574 mAh g^{-1} retained after 200 cycles. From Figure S6, the SiNR electrodes are largely intact after cycling, with only a small number of cracks. While for SiNP electrode, severe cracks occurred after cycling. In addition, some white patches appear in the SiNP electrode, indicating a deterioration of electrical contact. This proves that directional expansion characteristic of SiNR is also favourable for the stability of the electrode prepared from slurry.

The SiNR electrode exhibits a much higher initial coulombic efficiency (CE) (84.56%) than that of SiNP (70.3%), demonstrating a less Li loss of SiNR than that of SiNP. Li loss is generally believed to be resulted from the formation of SEI [54–57]. In fact, due to the the limited diffusion capability of Li, some Li will be trapped in the Si electrode. Li loss due to Li trapping in Si anode is an important but easily missed factor, which accounts for nearly 30% of the total initial Li loss [58–61]. The SiNR that we design enable the majority of Li^+ to transporting along <110> direction with the minimum energy barrier, which is also beneficial for reducing Li trapping. To better understand this anisotropic ionic conductivity, the cyclic voltammetry of (111), (100) and (110) Si-wafer was tested, respectively (Figure S3b-d). The typical cathodic peak at ~0.17 V and anodic peaks at ~0.35 V and ~0.51 V appear in all the three samples. The (111) Si-wafer performs the lowest peak current followed by (100) Si-wafer, with (110) Si-wafer topping the table in both cathodic and anodic branch. The experimental results are in agreement with the theoretical calculations (Fig. 1 c-h). On the other hand, from the differential capacity curve of the 1st cycle (Figure S3a), the SiNR electrode has a slightly higher lithium insertion potential and a slightly lower lithium removal potential than the SiNP electrode, further confirming a weaker energy barrier for Li migration in SiNR.

The SiNR electrode exhibits an outstanding long-cycle performance, retaining a specific capacity of 1721.3 mAh g^{-1} (~80% capacity retention) after 2000 cycles at a rate of 2 A g^{-1}. The initial CE is 83%, which exceeds 99% in the second cycle, indicating that an SEI layer forms at the first cycle and remains stable throughout the test. In contrast, due to the nondirective volume changes of the SiNP electrode during cycling, the SEI continuously rebuilds. The SiNP electrode has a marked capacity decay, retaining only 190 mAh g^{-1} after 1000 cycles (Fig. 5c). Moreover, the rate capabilities of the SiNR and the SiNP electrode were
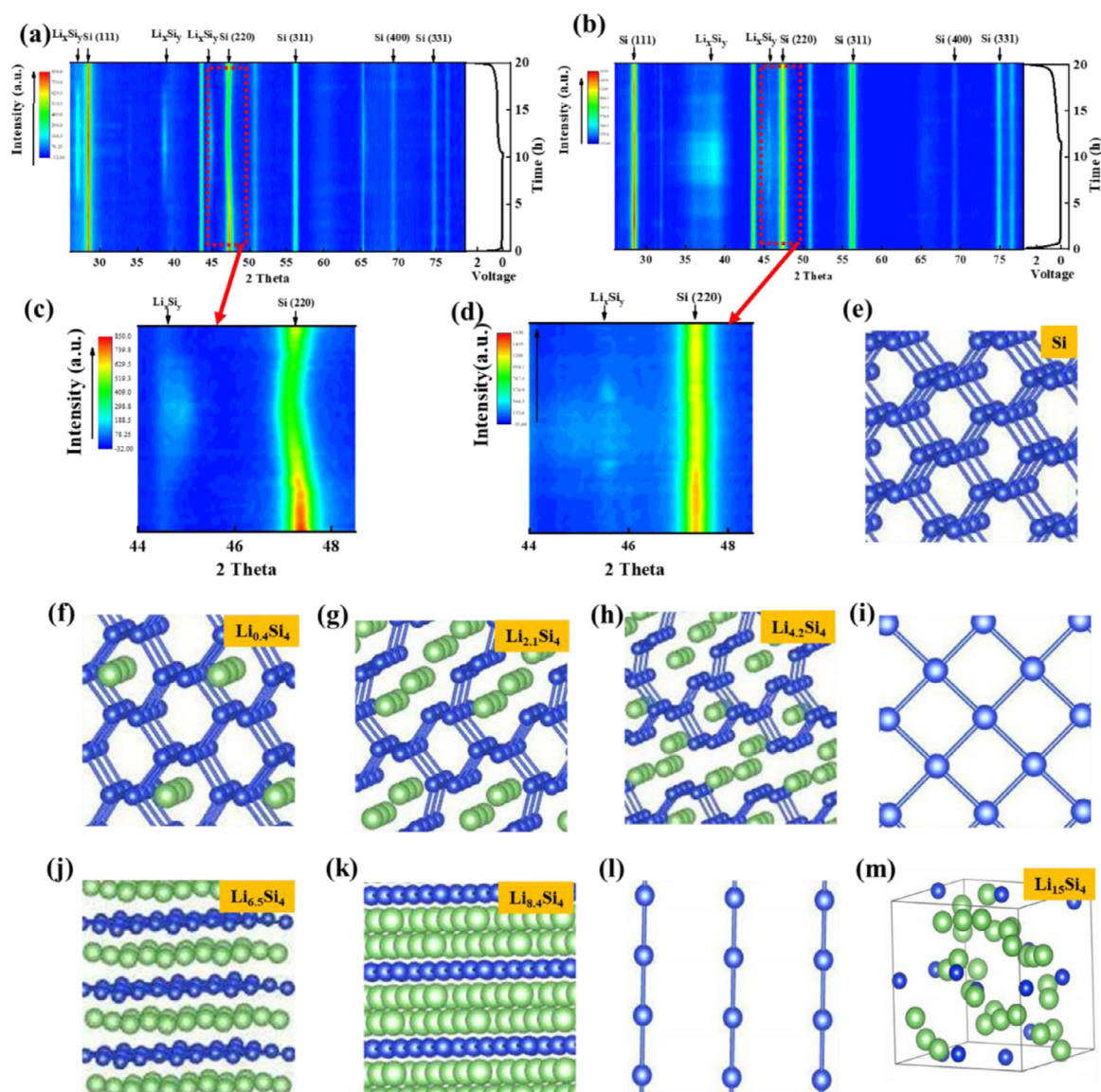
Fig. 4. Two-dimensional contour plots of *in situ* XRD for the structural evolution silicon nanoribbons (a, c), and silicon nanoparticles (b, d) anode during the first charge–discharge cycle at C/10 in a half cell. Theoretical calculations of the structural evolution during lithiation/delithiation processes: for SiNR before lithiation (e), and when the number of inserted Li increased to $Li_{0.4}Si_4$ (f), $Li_{2.1}/Si_4$ (g), $Li_{4.2}/Si_4$ (h), $Li_{6.5}/Si_4$ (i), and $Li_{8.4}/Si_4$ (k), respectively. (j) The two-dimensional square-like structure of Si lattice in $Li_{6.5}/Si_4$. (l) The chain structure of Si lattice in $Li_{8.4}/Si_4$. (m) Li_{15}/Si_4, the maximum amount of embedded lithium in bulk Si. Si and Li atoms are represented by blue and green balls, respectively.

evaluated in Fig. 5e with a stepwise current density programmed from 1 to 20 A g^{-1}. With the increase of the current density along the steps, the SiNR electrode shows a slower capacity decay than that of SiNP. Despite an extremely high rate of 20 A g^{-1}, the SiNR still shows a high capacity of ~1000 mAh g^{-1}, much higher than that of SiNP (~ 560 mAh g^{-1}), which is ascribed to the high Li mobility along <110> in the SiNR electrode. When the current density is set back, the capacity of the SiNR electrode can generally recover to the initial value. Over 1000 mA h g^{-1} after 2000 cycles at 10 A g^{-1} for the SiNR was measured in the end, demonstrating an excellent rate performance with long-cycle stability. Besides, as shown in Fig. 5d and f, the electrochemical impedance spectra (EIS) of the SiNR and SiNP at the state of charge (SOC) of 50% after 10, 500 and 1000 cycles were measured, respectively. The SiNR electrode shows much lower impedance than the SiNP electrode, indicative of faster charge transfer and higher electrode conductivity, consistent with the rate capability measurements of the SiNR and the SiNP electrodes (Fig. 5e). Unlike the SiNP electrode, the impedance of SiNR only

increases slightly in the process of cycling, consistent with its stable long cycle. To demonstrate the applicability of our electrode to practical applications, we assembled a full cell with a SiNR anode and a $LiCoO_2$ cathode (Fig. 5g). Considering the low initial Coulombic efficiency of 75%, we first prelithiated the SiNR anodes using half cells at 0.2 C for one cycle and then combined the SiNR and LCO electrodes into a full cell. The SiNR electrode exhibited a reversible capacity of 946 mA h g^{-1} (based on the weight of active materials in the anode) after 500 cycles, with 78% capacity retention at 1 A g^{-1}. In the rate performance, the full cell retains a high capacity of 921 mAh g^{-1} after 120 cycles at from 0.1 A g^{-1} to 2 A g^{-1} (Fig. 5h). As is shown in the inset of Fig. 5g, the full cell successfully ignites an LED array of the logo "SiNR", demonstrating the outstanding driving performance in practical applications.

To further analyze the relationship between formation mechanism and lithiation mechanism of SiNR, the electrochemical etching process belongs to electrolytic cells, while the lithiation process belongs to galvanic cells. The galvanic cell produces electric current based on a chemi-
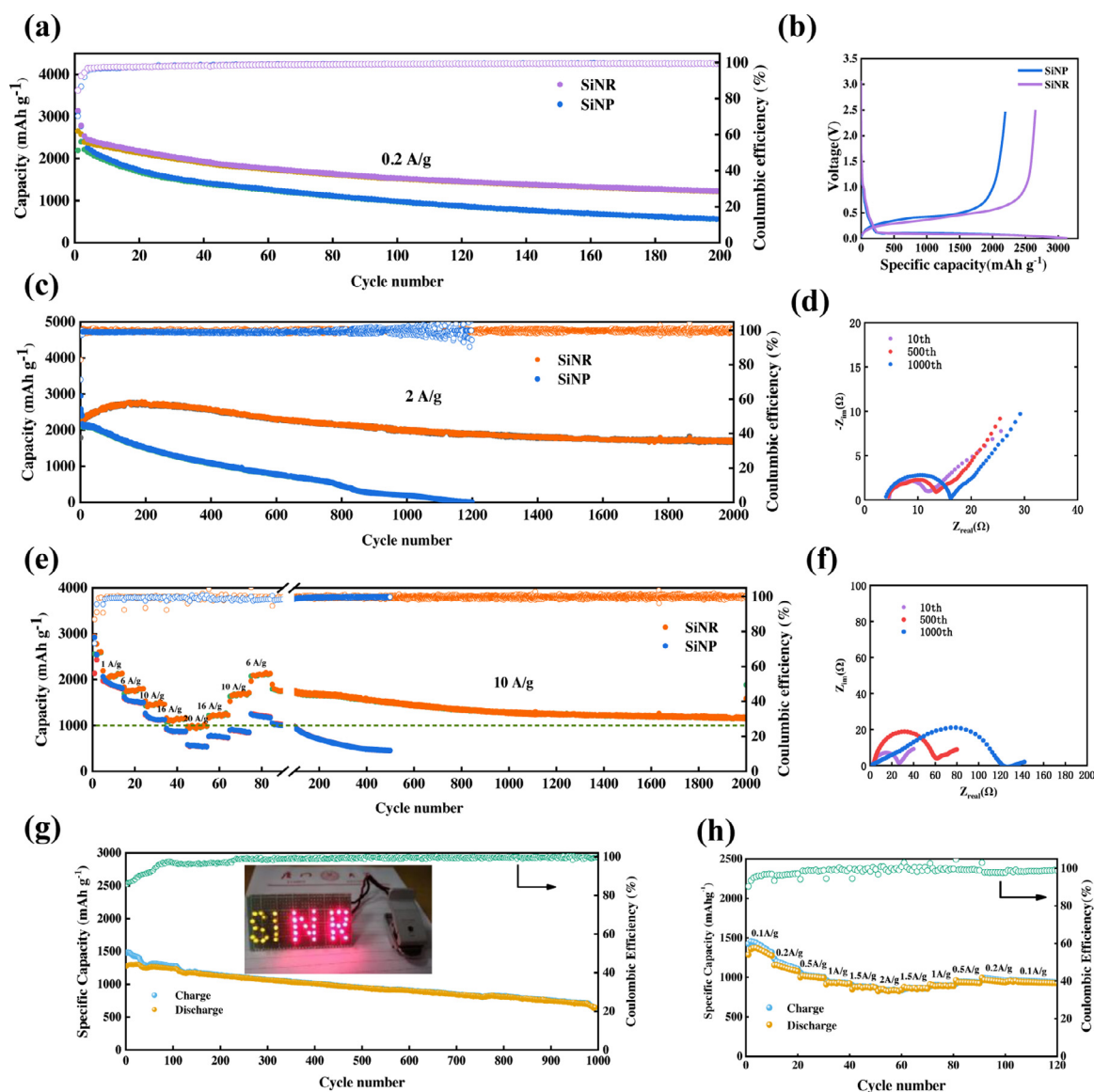
Fig. 5. (a) Specific capacity comparison SiNR and SiNP at 0.1C between 0.005 V and 2.5 V for 200 cycles. (b) Corresponding galvanostatic charge–discharge profiles at the 1st cycle. (c) Specific capacity of SiNP and SiNR at 2 A g^{-1} for 2000 cycles. Electrochemical impedance spectrum (EIS) of SiNR (d) and SiNP (f) with frequency ranging from 100 kHz to 0.01 Hz. (e) Rate performance of the SiNR and SiNP electrodes at various rates from 1 A g^{-1} to 20 A g^{-1} for 2000 cycles (All the electrodes were test at current densities of 0.2 A g^{-1} for the first two cycles). (g) Full-cell charge/discharge at 1 A g^{-1} with prelithiated SiNR anode and a LiCoO$_2$ cathode. (h) Rate performance of the full cell.

cal change that occurs spontaneously in it: the lithiated silicon anode expands in the direction of high electrochemical activity. The electrolytic cell does exactly the opposite. The electrode material treated by electrolytic cell system will improve its performance in a galvanic cell, which may probably be a general rule.

3. Conclusion

In this work, we have designed and synthesized the silicon nanoribbons with (110) crystal plane (SiNR) by a simple and low-cost electrochemical micromachining method. Benefiting from the directional migration of Li ions along <110>, directional expansion of lithiated SiNR along <110> and recrystallization of delithiated SiNR, the SiNR performs high ionic conductivity, high stable SEI and long cycling stability. No other modifications (such as carbon coating, prelithiation, doping, etc) for the SiNR are necessary. Our findings offer insights into a rational design of high-performance LIBs via exploiting the anisotropic

(de)lithiation mechanism of silicon experimentally and theoretically. The rational design of nanostructured battery materials and electrodes in this work also opens a new dimension in material design for other batteries bothering with similar challenges.

4. Experimental section

4.1. Synthesis of SiNR

P-type silicon (100) wafers with a resistance of 1– 10 Ω•cm were cut into squares (2 cm × 2 cm) and deposited with a 300 nm thick copper pad on the back. The etching solution contained HF (40 wt%) and dimethylformamide (DMF) with a volume ratio of 1:2. The electrochemical etching tank contained a copper plate electrode which was connected to the anode of constant-current source, a platinum wire counter electrode and a rubber ring with a diameter of 1.2 cm to guide the etching area. A constant current density of 22 mA cm^{-2} at room temperature

was applied to etch silicon wafers for 90 min. Then the current density was increased to 66 mA cm^{-2} for 30 min to peel off SiNR. The SiNR was subsequently cleaned by continuous washing in Milli-Q water (resistivity > 18MΩ cm) for 5 min and dried in a vacuum oven at 80 C for 12 h.

4.2. Characterization

To study the morphology evolution of SiNR during lithiation/delitiation, working electrode (WE) of SiNR was prepared by sputtering and tearing-off method. The silicon squares with SiNR were sputtered copper pads (300 nm) on the surface using magnetron sputtering equipment (SKY Technology Development Co. Ltd Chinese Academy of Sciences) (current 3.0 A, Argon flow rate 22 sccm). Subsequently, the copper pad was thickened to 300 μm by copper plating process in a plating tank. The copper pad was finally torn off and the working electrode with ends of SiNR rooting in copper collector was achieved.

The obtained samples were characterized by Scanning electron microscopy (SEM, Hitachi S4800, 15KV), and *in situ* transmission electron microscopy (Philips Tecnai F30), (FEI Tecnai G2 20 TEM). *In situ* X-ray Diffraction (XRD) patterns were collected at room temperature using a Bruker D8 Discover powder diffractometer and a Vantec500 detector with a 1 mm collimator. The active mass was weighted by a microbalance (METTLER TOLEDO XS3DU).

4.3. Electrochemical test

To test the electrochemical performance of the SiNR, a mixture of SiNR, acetylene black and carboxymethyl cellulose (CMC) in 70:15:15 in wt% of solid contents was ball milled to form a uniform slurry. The slurry was then coated on a copper foil with a diameter of 14 mm and dried at 80 °C overnight in a vacuum drying oven. The SiNP electrode was prepared at the same ratio. The mass loading of silicon on the copper foil was ~0.5 mg cm^{-2}, and the thickness of the active material is 15 μm. To assemble a half-cell, a CR2025 coin cell with a lithium foil used as the counter electrode was assembled in a glovebox (Mbraun, LABmaster 100, Germany, H$_2$O, O$_2$ < 0.1 ppm). The electrolyte solution was 1 M LiPF6 in ethylene carbonate (EC), dimethyl carbonate (DMC) and diethyl carbonate (DEC) (1:1:1 in volume) with 10% fluorinated ethylene carbonate (FEC) additive. The half-cells were tested over a voltage range of 0.005–2.5 V (versus Li$^+$/Li) at room temperature using a Land CT2001A system (Wuhan, China). Electrochemical impedance spectroscopy (EIS) was performed from 100 kHz to 10 mHz with 10 mV of amplitude on an electrochemical workstation (Shanghai Chenhua, CHI 660E). Cyclic voltammetry (CV) was tested at a scan rate of 0.2 mV s^{-1} over the potential window of 0.005 V-1.5 V. To assemble a full-cell, cathode electrodes consisting of LiCoO$_2$, SP, PVDF (80:10:10) were prepared. The full cells designed with an N/P ratio of 1.1 (the anode with an area capacity of 2 mAh/cm^2 and the cathode with an area capacity of 1.8 mAh/cm^2), were carried out in the voltage window beteen 2.5V and 4.1 V. The SiNR anodes were first prelithiated using half cells at 0.2 Ag^{-1} for two cycles to form a stable SEI.

4.4. Simulation

Our calculations have been performed by employing the Vienna *ab initio* simulation package (VASP) [62,63] which is based on the density functional theory (DFT) [xx] and the projector augmented wave (PAW) representation [64]. The Perdew-Burke-Ernzerhof (PBE) exchange-correlation energy functional [65] within the generalized gradient approximation (GGA) is employed in the calculations. The cutoff of plane-wave kinetic energy is set to be 500 eV. The Monkhorst-Pack scheme [66] with a 11×11×1 **k**-mesh was used to sample the Brillouin zone integration for the supercell. All the atoms in the systems were fully relaxed until the force on each atom was less than 0.02 eV/Å. The SiNR

was simulated by using a slab model that was comprised of 20 silicon layers and a vacuum spacing of about 20 Å between the Si slabs.

Author contribution statement

Songyan Chen and Ziqi Zhang designed the experiments and grasped the overall idea. Huiqiong Wang, Qiaobao Zhang and Yang He assisted with the *in situ* TEM. Meijuan Cheng and Zizhong Zhu carried out the theoretical calculation. Linshan luo and Pengfei Su involved in optimizing the electrochemical etching process. Xiang Han contributed to assembling the battery. Ziqi Zhang wrote the manuscript. Jianyuan Wang provided the experimental facilities guidance. Wei Huang and Cheng Li gave a unique insight.

Declaration of Competing Interest

The authors declare that they have no known competing financial interests or personal relationships that could have appeared to influence the work reported in this paper.

Supplementary materials

Supplementary material associated with this article can be found, in the online version, at doi:10.1016/j.ensm.2021.07.036.

References

[1] N.S. Choi, Z.H. Chen, S.A. Freunberger, X.L. Ji, Y.K. Sun, K. Amine, G. Yushin, L.F. Nazar, J. Cho, P.G. Bruce, Angew. Chem. Int. Edit. 51 (2012) 9994–10024.
[2] Y.X. Tang, Y.Y. Zhang, W.L. Li, B. Ma, X.D. Chen, Chem. Soc. Rev. 44 (2015) 5926–5940.
[3] M. Armand, J.M. Tarascon, Nature 451 (2008) 652–657.
[4] R. Schmuch, R. Wagner, G. Horpel, T. Placke, M. Winter, Nat. Energy 3 (2018) 267–278.
[5] M. Yoshio, T. Tsumura, N. Dimov, J. Power Sources 146 (2005) 10–14.
[6] M.N. Obrovac, L. Christensen, Electrochem. Solid State 7 (2004) A93–A96.
[7] G.Y. Zheng, S.W. Lee, Z. Liang, H.W. Lee, K. Yan, H.B. Yao, H.T. Wang, W.Y. Li, S. Chu, Y. Cui, Nat. Nanotechnol. 9 (2014) 618–623.
[8] J. Lu, Z.H. Chen, Z.F. Ma, F. Pan, L.A. Curtiss, K. Amine, Nat. Nanotechnol. 11 (2016) 1031–1038.
[9] M.T. McDowell, S.W. Lee, W.D. Nix, Y. Cui, Adv. Mater. 25 (2013) 4966–4984.
[10] C.J. Wen, R.A. Huggins, J. Solid State Chem. 37 (1981) 271–278.
[11] H. Li, X.J. Huang, L.Q. Chen, G.W. Zhou, Z. Zhang, D.P. Yu, Y.J. Mo, N. Pei, Solid State Ion. 135 (2000) 181–191.
[12] P. Limthongkul, Y.I. Jang, N.J. Dudney, Y.M. Chiang, Acta Mater. 51 (2003) 1103–1113.
[13] H. Li, X.J. Huang, L.Q. Chen, Z.G. Wu, Y. Liang, Electrochem. Solid State 2 (1999) 547–549.
[14] A. Magasinski, P. Dixon, B. Hertzberg, A. Kvit, J. Ayala, G. Yushin, Nat. Mater. 9 (2010) 461.
[15] W.-S. Kim, Y. Hwa, J.-H. Shin, M. Yang, H.-J. Sohn, S.-H. Hong, Nanoscale 6 (2014) 4297–4302.
[16] L.-F. Cui, R. Ruffo, C.K. Chan, H. Peng, Y. Cui, Nano Lett. 9 (2009) 491–495.
[17] M.T. McDowell, S.W. Lee, I. Ryu, H. Wu, W.D. Nix, J.W. Choi, Y. Cui, Nano Lett. 11 (2011) 4018–4025.
[18] Q.B. Zhang, H.X. Chen, L.L. Luo, B.T. Zhao, H. Luo, X. Han, J.W. Wang, C.M. Wang, Y. Yang, T. Zhu, M.L. Liu, Energy Environ. Sci. 11 (2018) 669–681.
[19] H. Wu, G. Chan, J.W. Choi, I. Ryu, Y. Yao, M.T. McDowell, S.W. Lee, A. Jackson, Y. Yang, L. Hu, Y. Cui, Nat. Nanotechnol. 7 (2012) 309–314.
[20] J. Wan, A.F. Kaplan, J. Zheng, X. Han, Y. Chen, N.J. Weadock, N. Faenza, S. Lacey, T. Li, J. Guo, L. Hu, J. Mater. Chem. A 2 (2014) 6051–6057.
[21] L.B. Chen, J.Y. Xie, H.C. Yu, T.H. Wang, J. Appl. Electrochem. 39 (2009) 1157–1162.
[22] Y. Zhang, B. Li, B. Tang, Z. Yao, X. Zhang, Z. Liu, R. Gong, P. Zhao, J. Alloys Compd. 846 (2020).
[23] G. Nava, J. Schwan, M.G. Boebinger, M.T. McDowell, L. Mangolini, Nano Lett. 19 (2019) 7236–7245.
[24] A. Magasinski, P. Dixon, B. Hertzberg, A. Kvit, J. Ayala, G. Yushin, Nat. Mater. 9 (2010) 353–358.

[25] H.P. Jia, X.L. Li, J.H. Song, X. Zhang, L.L. Luo, Y. He, B.S. Li, Y. Cai, S.Y. Hu, X.C. Xiao, C.M. Wang, K.M. Rosso, R. Yi, R. Patel, J.G. Zhang, Nat. Commun. 11 (2020) 9.

[26] J.R. Szczech, S. Jin, Energy Environ. Sci. 4 (2011) 56–72.

[27] Z. Sun, S. Tao, X. Song, P. Zhang, L. Gao, J. Electrochem. Soc. 162 (2015) A1530–A1536.

[28] Z.Q. Zhang, X. Han, L.C. Li, P.F. Su, W. Huang, J.Y. Wang, J.F. Xu, C. Li, S.Y. Chen, Y. Yang, J. Power Sources (2020) 450.

[29] J. Li, X. Xiao, Y.-T. Cheng, M.W. Verbrugge, J. Phys. Chem. Lett. 4 (2013) 3387–3391.

[30] J. Li, Y. Wang, Z. Huang, K. Huang, X. Qi, J. Zhong, J. Mater. Sci.-Mater. Electron. 27 (2016) 12813–12819.

[31] Y. Hwa, W.-S. Kim, B.-C. Yu, S.-H. Hong, H.-J. Sohn, J. Phys. Chem. C 117 (2013) 7013–7017.

[32] M.D. Fleischauer, M.N. Obrovac, J.R. Dahn, J. Electrochem. Soc. 155 (2008) A851–A854.

[33] B.A. Boukamp, G.C. Lesh, R.A. Huggins, J. Electrochem. Soc. 128 (1981) 725–729.

[34] X.H. Liu, H. Zheng, L. Zhong, S. Huan, K. Karki, L.Q. Zhang, Y. Liu, A. Kushima, W.T. Liang, J.W. Wang, J.H. Cho, E. Epstein, S.A. Dayeh, S.T. Picraux, T. Zhu, J. Li, J.P. Sullivan, J. Cumings, C.S. Wang, S.X. Mao, Z.Z. Ye, S.L. Zhang, J.Y. Huang, Nano Lett. 11 (2011) 3312–3318.

[35] Y. He, X.Q. Yu, Y.H. Wang, H. Li, X.J. Huang, Adv. Mater. 23 (2011) 4938–4941.

[36] Y. He, X.Q. Yu, G. Li, R. Wang, H. Li, Y.L. Wang, H.J. Gao, X.J. Huang, J. Power Sources 216 (2012) 131–138.

[37] M.J. Chon, V.A. Sethuraman, A. McCormick, V. Srinivasan, P.R. Guduru, Phys. Rev. Lett. (2011) 107.

[38] X.H. Liu, L. Zhong, S. Huang, S.X. Mao, T. Zhu, J.Y. Huang, ACS Nano 6 (2012) 1522–1531.

[39] S.W. Lee, M.T. McDowell, J.W. Choi, Y. Cui, Nano Lett. 11 (2011) 3034–3039.

[40] S.W. Lee, M.T. McDowell, L.A. Berla, W.D. Nix, Y. Cui, P. Natl. Acad. Sci. USA, 109 (2012) 4080–4085.

[41] J.L. Goldman, B.R. Long, A.A. Gewirth, R.G. Nuzzo, Adv. Funct. Mater. 21 (2011) 2412–2422.

[42] X.H. Liu, J.W. Wang, S. Huang, F.F. Fan, X. Huang, Y. Liu, S. Krylyuk, J. Yoo, S.A. Dayeh, A.V. Davydov, S.X. Mao, S.T. Picraux, S.L. Zhang, J. Li, T. Zhu, J.Y. Huang, Nat. Nanotechnol. 7 (2012) 749–756.

[43] F. Kong, R. Kostecki, G. Nadeau, X. Song, K. Zaghib, K. Kinoshita, F. McLarnon, J. Power Sources 97–8 (2001) 58–66.

[44] M. Schnabel, S.P. Harvey, E. Arca, C. Stetson, G. Teeter, C.M. Ban, P. Stradins, ACS Appl. Mater. Inter. 12 (2020) 27017–27028.

[45] J. Shin, K. Park, W.H. Ryu, J.W. Jung, I.D. Kim, Nanoscale 6 (2014) 12718–12726.

[46] S.C. Wu, K. Zhu, J. Tang, K.M. Liao, S.Y. Bai, J. Yi, Y. Yamauchi, M. Ishida, H.S. Zhou, Energy Environ. Sci. 9 (2016) 3262–3271.

[47] C.K. Chan, H. Peng, G. Liu, K. McIlwrath, X.F. Zhang, R.A. Huggins, Y. Cui, Nat. Nanotechnol. 3 (2008) 31–35.

[48] J.W. Choi, D. Aurbach, Nat. Rev. Mater. 1 (2016).

[49] N. Liu, H. Wu, M.T. McDowell, Y. Yao, C. Wang, Y. Cui, Nano Lett. 12 (2012) 3315–3321.

[50] H. Wu, Y. Cui, Nano Today 7 (2012) 414–429.

[51] W.-J. Zhang, J. Power Sources 196 (2011) 13–24.

[52] T.D. Hatchard, J.R. Dahn, J. Electrochem. Soc. 151 (2004) A838–A842.

[53] X.H. Liu, H. Zheng, L. Zhong, S. Huan, K. Karki, L.Q. Zhang, Y. Liu, A. Kushima, W.T. Liang, J.W. Wang, J.-H. Cho, E. Epstein, S.A. Dayeh, S.T. Picraux, T. Zhu, J. Li, J.P. Sullivan, J. Cumings, C. Wang, S.X. Mao, Z.Z. Ye, S. Zhang, J.Y. Huang, Nano Lett. 11 (2011) 3312–3318.

[54] H.J. Kim, S. Choi, S.J. Lee, M.W. Seo, J.G. Lee, E. Deniz, Y.J. Lee, E.K. Kim, J.W. Choi, Nano Lett. 16 (2016) 282–288.

[55] M. Ko, S. Chae, J. Ma, N. Kim, H.W. Lee, Y. Cui, J. Cho, Nat. Energy 1 (2016).

[56] C. Xu, F. Lindgren, B. Philippe, M. Gorgoi, F. Bjorefors, K. Edstrom, T. Gustafsson, Chem. Mater. 27 (2015) 2591–2599.

[57] J. Zhao, Z.D. Lu, N.A. Liu, H.W. Lee, M.T. McDowell, Y. Cui, Nat. Commun. 5 (2014).

[58] D. Rehnlund, F. Lindgren, S. Bohme, T. Nordh, Y.M. Zou, J. Pettersson, U. Bexell, M. Boman, K. Edstrom, L. Nyholm, Energy Environ. Sci. 10 (2017) 1350–1357.

[59] A.L. Michan, G. Divitini, A.J. Pell, M. Leskes, C. Ducati, C.P. Grey, J. Am. Chem. Soc. 138 (2016) 7918–7931.

[60] K. Ogata, E. Salager, C.J. Kerr, A.E. Fraser, C. Ducati, A.J. Morris, S. Hofmann, C.P. Grey, Nat. Commun. 5 (2014).

[61] B. Zhu, G.L. Liu, G.X. Lv, Y. Mu, Y.L. Zhao, Y.X. Wang, X.Q. Li, P.C. Yao, Y. Deng, Y. Cui, J. Zhu, Sci. Adv. 5 (2019).

[62] G. Kresse, J. Furthmuller, Phys. Rev. B 54 (1996) 11169–11186.

[63] G. Kresse, J. Furthmuller, Comput. Mater. Sci. 6 (1996) 15–50.

[64] P.E. Blochl, Phys. Rev. B 50 (1994) 17953–17979.

[65] J.P. Perdew, K. Burke, M. Ernzerhof, Phys. Rev. Lett. 77 (1996) 3865–3868.

[66] H.C. Chow, S.H. Vosko, Can. J. Phys. 58 (1980) 497–503.